journal

J. Am. Ceram. Soc., **85** [6] 1505–11 (2002)

Weight Function Analysis on the R-Curve Behavior of Multilayered Alumina–Zirconia Composites

Robert J. Moon and Mark Hoffman*

School of Materials Science and Engineering, The University of New South Wales, New South Wales 2052, Australia

Jon Hilden, Keith Bowman,*,** and Kevin Trumble*

School of Materials Engineering, Purdue University, West Lafayette, Indiana 47907

Jürgen Rödel*

Department of Materials Science, University of Technology–Darmstadt, D-64287 Darmstadt, Germany

The single-edge V-notched-beam (SEVNB) testing geometry was used to measure the crack growth resistance (*R*-curve) behavior of multilayered alumina–zirconia composites. Fracture mechanics weight function analysis was applied to predict the *R*-curve behavior of multilayered composites having a stepwise change in composition. These results were then used to differentiate the influence of residual stresses from crack-bridging stresses on the measured *R*-curve behavior.

I. Introduction

RESIDUAL thermal stresses associated with thermal expansion mismatch between layers in a ceramic–ceramic composite can have a significant influence on fracture behavior. Specifically, residual compressive forces on the outer surfaces can increase the apparent fracture toughness by adding a closure stress to surface flaws.[1,2] Processing techniques that produce layered structures within a sample allow one to control the residual stress distribution throughout the composite.[3,4] By alternating layers of residual compressive and tensile stresses[3,4] and by varying the magnitude of the residual stress within these layers, various composite fracture behaviors can be achieved.[4–8] Thus, the measured fracture toughness (K_{IC}) and crack growth resistance behavior (*R*-curve), which depend on microstructure and residual stress, become functions of position within the composite.[1,2,3,6,9–11] Pertinent studies by Lakshminarayanan *et al.*[1] and Marshall *et al.*[3] are described in further detail.

Lakshminarayanan *et al.*[1] used several single-edge notched-beam (SENB) samples with various notch depths to investigate the fracture behavior of trilayered alumina–zirconia composites where the outer layers had ~600 MPa residual compressive stress and the inner layer had ~100 MPa residual tensile stress. The composite K_{IC} increased from 12 to ~30 MPa·m$^{1/2}$ as the notch depth approached the thickness of the outer surface layer (0.8 mm) and then monotonically decreased to ~13 MPa·m$^{1/2}$ as the notch depth was increased into the inner layer. Because the measured K_{IC} values of the monolithic samples of the individual layer compositions were 5 and 7 MPa·m$^{1/2}$, an improvement in the composite K_{IC} by tailoring the residual stresses was demonstrated.

Marshall *et al.*[3] used the single-edge precracked-beam (SEPB) testing method for evaluating the *R*-curve behavior of a multilayered alumina–zirconia composite that contained 19 alternating ceria-stabilized zirconia (100Z) and 50-vol%-alumina–50-vol%-ceria–zirconia layers (50Z), each 35 μm thick, in the center of a beam of ceria–zirconia. The initial ~550 μm precrack and the further ~450 μm of crack extension (total crack length of ~1000 μm) were within the outer ceria–zirconia region of the sample and resulted in increased apparent fracture toughness (K_R) from ~4.2 to 5 MPa·m$^{1/2}$. With crack extensions into the layered region of the sample, the K_R increased stepwise, reaching a maximum of ~17.5 MPa·m$^{1/2}$. The results demonstrated that the addition of the 50Z layers had a significant influence on the measured *R*-curve.

When measuring the *R*-curve behavior of either multilayered or gradient composites, the ability to differentiate between microstructure-related toughening mechanisms (i.e., crack bridging, kinking, and transformation toughening) and residual-stress-based mechanisms is difficult. The study by Lakshminarayanan *et al.*[1] experimentally demonstrates that fracture mechanical weight function analysis can be used to effectively estimate the composite fracture toughness as a function of position within a layered composite containing macroscopic residual stresses.

The purpose of the present study is to use the weight function analysis to distinguish the effects of residual stress distributions from the crack-bridging closure stresses on the measured *R*-curve behavior of a multilayered alumina–zirconia composite.

II. Experimental Procedure and Analysis

(1) Sample Preparation

Multilayered alumina–zirconia composites were produced using sequential centrifugal consolidation[12–15] of a coagulated[12,16] aqueous alumina–zirconia suspension. Further details on the centrifugal consolidation and the suspension preparation procedure can be found in Ref. 9. The solids compositions of the suspension used in this study are described in Table I. The composite green bodies were dried and then fired at 1600°C for 4 h in air with 250°C/h heating and cooling ramp rates. Sintered disks were produced measuring ~6 cm diameter by ~1 cm thickness and containing <5% porosity.

Sintered disks were surface ground flat using a 600 grit diamond wheel, and multiple bend bars measuring 4 mm × 3 mm × 35 mm were cut from the center of each disk. A V-notch was cut across the 3 mm × 35 mm face, perpendicular to the

D. B. Marshall—contributing editor

Manuscript No. 188201. Received October 20, 2000; approved February 25, 2002.
Presented at the 102nd Annual Meeting of The American Ceramic Society, St. Louis, MO, May 1, 2000 (Fibrous Monoliths and Oxide/Non-oxide Composites: Processing and Mechanical Properties Session of the Ceramic Matrix Composites Symposium, Paper No. B2–055-00).
Based in part on the Ph.D. thesis submitted by R. J. Moon, School of Materials Engineering, Purdue University, West Lafayette, IN, 2000.
Supported by the U.S. Army Research Office under MURI Grant No. DAAH04–96-1–0331.
*Member, American Ceramic Society.
**Fellow, American Ceramic Society.

Table I. Suspension Compositions

Suspension	Composition (vol% solids)	Composition nomenclature
A	90 alumina† + 10 zirconia‡	90Al
B	80 alumina† + 20 zirconia‡	80Al

†A16SG, 99.8%, D_{50} = 0.4 μm, ALCOA, Bauxite, AR. ‡CEZ-12 (mol%), 98%, D_{50} = 0.4 μm, American Vermiculite Corp., Marietta, GA.

length of the bend bar, as described in previous work.[10,17] The V-notch tip radii (ρ) were measured to be 5–10 μm using optical microscopy. The 4 mm × 35 mm side surfaces were additionally polished with 15 μm diamond abrasives, which provided a surface finish that was sufficient for crack growth observations.

Monolithic and layered samples were produced (Table II). The monolithic 80-vol%-alumina–20-vol%-zirconia (80Al) sample was used to measure the *R*-curve behavior without the influence of a macroscopic thermal residual stress distribution. The layered sample, consisting of five alternating 80Al/90Al compositional layers, was used to measure the *R*-curve behavior influenced by a thermal residual stress distribution (Fig. 1). The Young's modulus (*E*), Poisson's ratio (*ν*), and coefficient of thermal expansion (CTE, α) for the 80Al and 90Al compositions were estimated by taking the geometric average of the upper (equal strains) and lower (equal stress) bounds of the rule-of-mixtures models and are shown in Table III. Because the material properties must lie between the upper and lower bounds, the errors in these estimates are believed to be <5%.

(2) Mechanical Testing

Direct observations of crack initiation and extension were made on the bend bar side surfaces using a specialized four-point bend fixture placed on the stage of an optical microscope.[9,10,18] Loading was achieved using a piezoelectric translator and measured using a miniature load cell. A fluorescent dye penetrant (Met-L-Clek FP 90, Helling KG, GmbH, Hamburg, Germany) and an ultraviolet light source were used to measure crack lengths. The fluorescent dye was in contact with the V-notch tip during crack initiation and was within the crack during every subsequent crack extension. For slow crack extensions, the fluorescent dye immediately penetrated into the newly extended crack, allowing crack extensions to be observed. There was no measurable influence of the fluorescent dye on crack extension.[11]

Samples were tested under displacement control, where subcritical crack initiation and further crack extensions (~10 μm increments) were achieved by loading at a slow rate. The incremental loading technique used is described elsewhere.[9,10] The applied load to instigate crack propagation (P_c) and total flaw length (*a*) were measured, and, for each crack extension, the apparent K_R was calculated as outlined below.

(3) Weight Function Analysis

Bueckner[19] showed that the stress-intensity factor (*K*) for an edge crack of depth *a* can be calculated by integrating the product of a weight function ($h(x,a)$) and any stress distribution ($\sigma(x)$) acting normal to the fracture plane over the crack length:

$$K = \int_0^a h(x,a)\sigma(x)\,dx \tag{1}$$

where *x* is the distance along the crack, measured from the surface. The weight function used must be derived for a specific crack-component configuration.

In the work of Fett and Munz[20,21] and Fett,[22] a weight function for an SENB sample and notch geometry is given by

$$h(x,a) = \left(\frac{2}{\pi a}\right)^{1/2} \frac{1}{\left(1-\frac{x}{a}\right)^{1/2}\left(1-\frac{a}{W}\right)^{3/2}} \times \left[\left(1-\frac{a}{W}\right)^{3/2} + \sum A_{\nu\mu}\left(1-\frac{x}{a}\right)^{\nu+1}\left(\frac{a}{W}\right)^{\mu}\right] \tag{2}$$

where *a* is the total flaw length measured from the bend bar tensile surface and *W* the sample width, as shown in Fig. 1(b). The values of the coefficients $A_{\nu\mu}$ and the exponents ν and μ are given in Refs. 20 and 21. It has been demonstrated in elastically graded samples, having a 33% variation in elastic modulus (i.e., E_{max}/E_{min} = 1.33) across the graded region, that the discrepancy in stress intensity factors calculated using a weight function that considers an elasticity gradient and one that does not is <10%.[23,24] In the current study, the elasticity variation of E_{90}/E_{80} = 1.06 within the layered sample must, therefore, result in errors of <10% when calculating the stress intensity factors.

(4) Stress Distribution

Three independent stress distributions were considered in this study: an applied bending stress distribution; a residual thermal stress distribution; and a bridging closure stress distribution. The applied bending stress distribution for the monolithic sample ($\sigma^h_{bend}(x,P)$) was estimated using a standard bending-stress formula for homogeneous materials:

$$\sigma^h_{bend}(x,P) = \frac{1.5P(S_o - S_i)}{BW^2}\left(1-\frac{2x}{W}\right) \tag{3a}$$

where *P* is the applied load, S_o and S_i the outer and inner support spans of the four-point bending fixture (in this study, 20 and 10 mm, respectively), *B* the sample thickness, and *W* the sample width.

The applied bending stress distribution for the layered sample ($\sigma_{bend}(x,P)$) is calculated using a modified bending stress formula in which the influence of the modulus variation across the bend bar cross section is considered. The derivation is shown in Ref. 25.

Table II. List of Samples Tested

Sample	Characteristic investigated	Number of deposits† (suspension)	Deposit thickness (μm)	Layer offset‡ (μm)	Sample cross section (mm)		V-notch depth (μm)
					B	*W*	
Monolithic 80AL	Monolithic properties	1 (B)			3.01	4.02	1050
Layered	Stepwise residual stress	2 (B)	~350	10	2.68	4.08	1175
		5 (B)	~180				
		1 (A)§	~180				
		1 (B)	~700				
		1 (A)§	~180				
		5 (B)	~180				
		1 (B)	~350				

†Number of deposits observed within the bend bar shown in Fig. 1. ‡See Ref. 10 for definition and relevancy. §Residual compression layer.

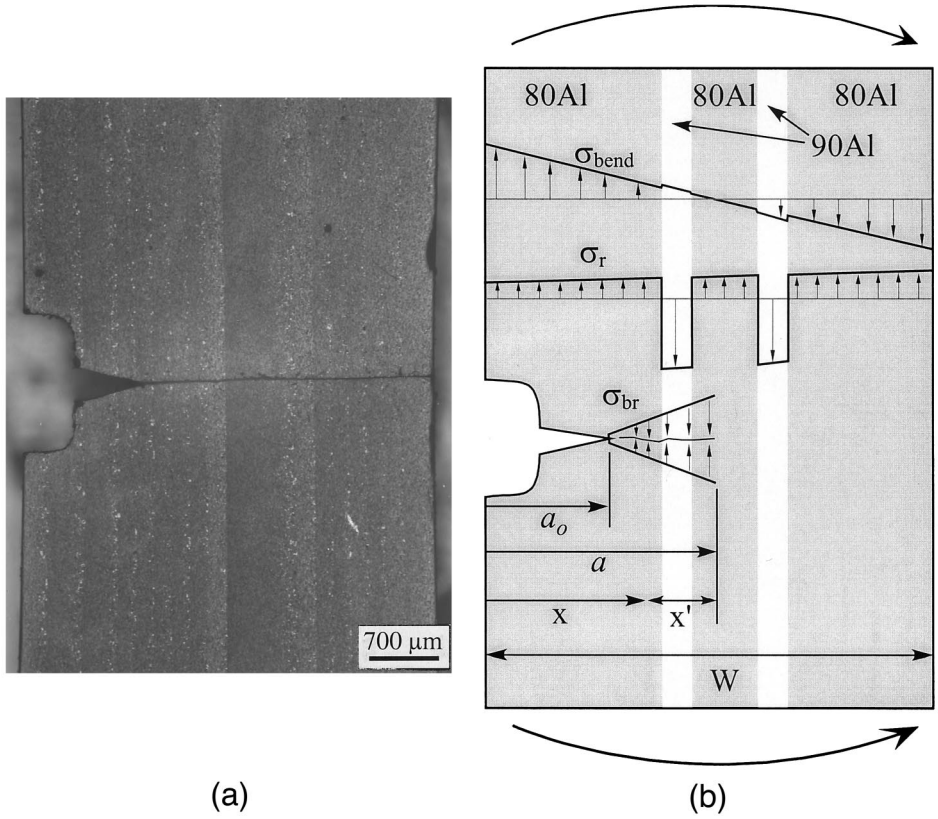

Fig. 1. Layered sample: (a) optical micrograph of the postcracked SEVNB sample showing the layer stacking with respect to the V-notch and (b) schematic of the stress distribution showing the three independent stress components, bending ($\sigma_{bend}(x)$), residual stress ($\sigma_r(x)$), and bridging ($\sigma_{br}(x,a)$).

Table III. Composition Properties

Composition (vol%)	E (GPa)	ν	α (10^{-6}/°C)
100 Al_2O_3	380[†]	0.25[‡]	8.39[†]
90Al	356[§]	0.26[§]	8.66[§]
80Al	335[§]	0.26[§]	8.94[§]
100 *t*-ZrO_2	205[†]	0.32[†]	11.5[†]

[†]Reference 40. [‡]Reference 41. [§]Values were calculated by geometric average of the upper and lower bounds of the rule-of-mixture.

The resulting equation can be used for any elasticity variation across a bend bar sample geometry tested in four-point bending:

$$\sigma_{bend}(x) = \frac{P}{4B}(S_o - S_i)E'(x)\frac{E_2 - E_1 x}{E_2^2 - E_1 E_3} \tag{3b}$$

where $E'(x)$ is the plane strain variation of modulus across the sample cross section and E_1, E_2, and E_3 are given in the Appendix.

The residual thermal stress distribution ($\sigma_r(x)$) within the monolithic sample was zero. For the layered sample, $\sigma_r(x)$ was estimated from the thermal expansion mismatch strains resulting from the variations of $E(x)$, $\nu(x)$, and $\alpha(x)$ across the sample. Moreover, the influences of tile warping that would result from nonsymmetrical stacking of the compositional layers within the tile were taken into account. The derivation is shown in Ref. 25.

$$\sigma_r(x) = \Delta T E'(x)\left(\alpha(x) + \frac{-A_1E_2x + A_2E_1x + A_1E_3 - A_2E_2}{E_2^2 - E_1E_3}\right) \tag{4}$$

where A_1, A_2, E_1, E_2, and E_3 are given in the Appendix, and ΔT is the temperature range over which the thermal stresses develop. When cooling from the sintering temperature to ~1250°C, the thermal stresses formed within the sample were believed to be relieved via creep,[26,27] and, thus, $\Delta T = 1225$°C was estimated as a result of the cooling from 1250°C to 25°C. Additional calculations using $\Delta T = 1125°$ and 1325°C were also made.

The bridging stress distribution that acts along a given crack length is dependent on the crack opening displacement (COD) along the crack length. For monolithic ceramic materials, the bridging stress distribution ($\sigma_{br}(u)$) is taken to have an empirical power-law form similar to that that has been used previously:[28–34]

$$\sigma_{br}(u) = \sigma_{max}\left(1 - \frac{u}{u^*}\right)^n \tag{5}$$

where $2u$ is the COD, σ_{max} the maximum stress supported by the bridging zone, n a softening coefficient, and $2u^*$ the COD in which closure stresses resulting from interlocking grains stop contributing to the bridging stress. Equation (5) assumes that the bridging stress decreases as the COD increases, which is solely attributed to the geometrical influence of the decreasing bridging area (or number of grains that can bridge the crack) as the crack faces separate.[30–32] For alumina composites, the studies by Rödel *et al.*[31] and Hay and White[32] have demonstrated that the bridging stresses decrease as COD increases, and, thus, the bridging stress decreases for increasing distance behind the crack tip.

For the weight function calculation used in this study, it was necessary to express the bridging stress function in Eq. (5) as a function of distance behind the crack tip. The COD was related to the distance behind the crack tip (x') using the Irwin K-field plane-strain displacement relation ($u(x')$) developed by Barenblatt[35] for homogeneous materials:

$$\text{COD} = 2u(x') = 2\left[\left(\frac{8x'}{\pi}\right)^{1/2}\frac{K_o}{E/(1-\nu^2)}\right] \tag{6}$$

where K_o is the intrinsic stress intensity factor and represents a lower bound for COD.[31] Because E is considered constant, the

variation in E across the layered sample of ~6% results in small errors in the calculated COD.

Equation (5) is expressed as a function of x' by substituting Eq. (6) for u and u^*. For the u substitution, x' is replaced with $a - x$, and, for the u^* substitution, x^* is replaced with the steady-state bridging zone length (L), i.e., the critical distance behind the crack tip, in which the COD is large enough that closure stresses resulting from interlocking grains are zero. The resulting equation relates the bridging stress as a function of distance behind the crack tip ($\sigma_{br}(x,a)$):

$$\sigma_{br}(x,a) = \sigma_{max}\left[1 - \left(\frac{a-x}{L}\right)^{1/2}\right]^n \quad (7)$$

where $a - x$ is the distance from the crack tip.

Figure 1(b) shows the three stress distributions, σ_{bend}, σ_r, and σ_{br}, within the layered sample loaded in four-point bending.

(5) Measured Stress Intensity Factors

The weight function analysis was used to calculate the K_R from experimental data, i.e., the critical applied load to further extend a crack (P_c) and the average total flaw length ($a = (a_A + a_B)/2$) measured from each side (A and B) of the sample. a_A and a_B are the sum of the V-notch depth (a_o) and the crack extension as measured on sides A and B of the bend bar.[10]

For the monolithic sample, K_R values were calculated by substituting a standard bending stress formula, Eq. (3*a*), into Eq. (1). K_R was then calculated for each P_c vs a data point obtained from the experiment. The procedure for the layered sample was similar, except that the modified bending stress formula, Eq. (3*b*), was substituted into Eq. (1) to account for the influences of the changing modulus across the sample. In each case, the K_R values were those one would measure without previous knowledge of residual thermal stresses or crack-bridging stresses.

(6) Calculated Stress Intensity Factors

The stress intensity factors associated with each stress distribution were independently defined using the weight function analysis. The applied stress intensity factor for the monolithic sample ($K_a^m(x,P)$) was calculated with Eq. (3*a*) substituted into Eq. (1), whereas the layered sample ($K_a^L(x,P)$) was calculated with Eq. (3*b*) substituted into Eq. (1). The stress intensity factor resulting from the residual stress distribution acting along the total flaw length ($K_r(x)$) was calculated with Eq. (4) substituted into Eq. (1). The range of integration was from 0 to a. For $K_r(x) < 0$, the residual stress distribution produces crack shielding by decreasing the net crack-tip stress intensity, thus toughening the composite. The opposite is the case for $K_r(x) > 0$.

The stress intensity factor resulting from the bridging stress distribution acting along the crack length for the monolithic and layered samples ($K_{br}(a,a_o)$) was calculated with Eq. (7) substituted into Eq. (1). Bridging stresses were considered to act only along the extended crack length, i.e., the region defined by $a_o < x < a$, and, thus, the range of integration was from a_o to a. The bridging stress distribution resulted in $K_{br}(a,a_o) < 0$ for all crack extensions and, thus, led to toughening of the composite by decreasing the net crack-tip stress intensity factor.

(7) Stress Intensity Calculations

The effects of residual stress and crack bridging on the stress intensity factor at the crack tip (K_{tip}) were determined using the principle of superposition to sum K_a, K_r, and K_{br}:

$$K_{tip} = K_a + K_r + K_{br} \quad (8)$$

Because crack extension occurs when K_{tip} equals the intrinsic crack-tip toughness (K_o) it is possible to predict values for K_a (as a function of a) that cause crack extension. In this case, K_a is the same as K_R. Solving Eq. (8) for K_a, relabeling K_a to K_R, and replacing K_{tip} with K_o gives

$$K_R(a,a_o) = K_o(a) - K_r(a) - K_{br}(a,a_o) \quad (9)$$

The $K_o(a)$ values used were based on extrapolations of the 80Al and 90Al measured R-curves to the y-axis, in which the intrinsic fracture toughness values of $K_o^{80Al} = 3.6$ MPa·m$^{1/2}$ and $K_o^{90Al} = 3.2$ MPa·m$^{1/2}$ (Ref. 9) were obtained. The stress intensity factors obtained using this technique were believed to give a reasonable estimate for K_o, because the effects of crack-tip shielding and bridging were minimized.

The $K_r(a)$ and $K_{br}(a,a_o)$ profiles, which are independent of the applied load, were simply calculated for a. Figure 2 shows the three independent stress intensity factor profiles K_o, K_r, and K_{br} as function of position within the layered sample. K_r was calculated using material properties given in Table III and a $\Delta T = 1225$°C.

III. Results

(1) Monolithic Sample

The 80Al monolithic sample microstructure and R-curves are shown in Fig. 3. The plot consists of three curves: the measured R-curve; the calculated K_R profile; and the estimated intrinsic crack-tip toughness, $K_o^{80Al} = 3.6$ MPa·m$^{1/2}$. The measured stress intensity factor for crack initiation from the V-notch (K_i) was 4.0 MPa·m$^{1/2}$, in which the discrepancy between K_i and K_o^{80Al} was attributed to the relatively blunt ($\rho = 5$ μm) starter notch tip. The fracture mode was predominately intergranular, where bridging tractions were believed to be dominated by frictional pullout of interlocking grains. Transformation toughening of the 20 vol% zirconia was believed to be negligible because of the small amount of monoclinic zirconia detected (as compared with the tetragonal phase) on the fractured surface via X-ray diffractometry.[11] Moreover, microcrack process zones were not observed.[36]

The R-curve had a 0.8 MPa·m$^{1/2}$ increase in K_R over an ~700 μm crack extension. By fitting Eq. (9) to the experimentally measured data for the 80Al monolithic sample, with $K_r = 0$ (no residual stress), best fit values for σ_{max}, n, and L in the bridging function, Eq. (7), were found to be 19 MPa, 0.6, and 900 μm, respectively.

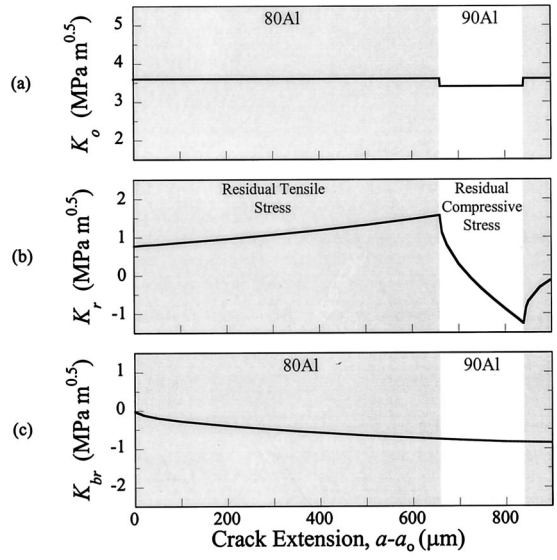

Fig. 2. Schematic of the estimated stress intensity factors as a function of position within the layered sample: (a) K_o, (b) K_r ($\Delta T = 1225$°C), and (c) K_{br}.

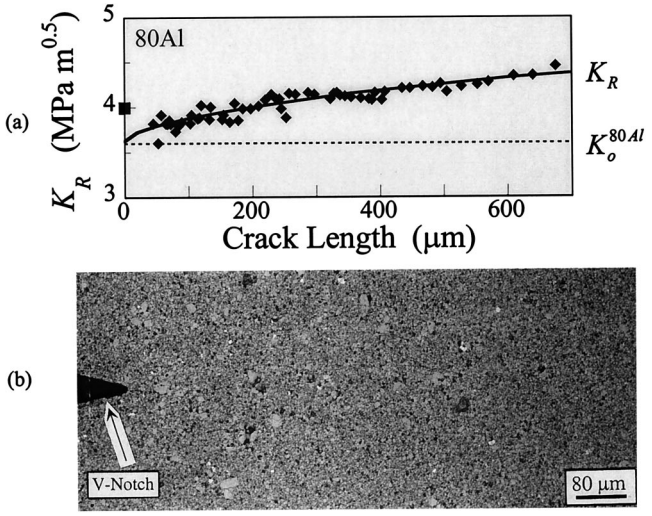

Fig. 3. 80Al monolithic sample: (a) (♦) experimentally measured *R*-curve with the calculated K_R and K_o^{80Al} profiles ((■) K_i for crack initiation from the V-notch tip), and (b) optical micrograph of the posttested sample showing the microstructure through which the crack propagated.

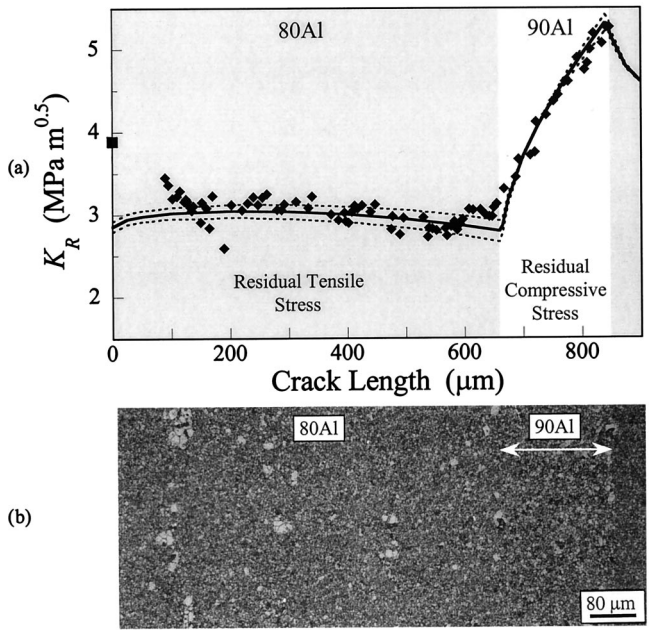

Fig. 4. Layered sample: (a) (♦) experimentally measured *R*-curve with three calculated K_R profiles ((—) K_R profile calculated with $\Delta T = 1225°C$ (in Eq. (4)), (- - -) influence of a $\pm 100°C$ variation of the ΔT estimate, and (■) K_i for crack initiation from the V-notch tip), and (b) optical micrograph showing the microstructure through which the crack propagated.

(2) Layered Sample

The layered sample microstructure, the measured *R*-curve, and the calculated K_R profile are shown in Fig. 4. The measured stress intensity factor for crack initiation from the V-notch (K_i) is 3.9 MPa·m$^{1/2}$. Initially, the measured *R*-curve has a negative slope, decreasing from 3.1 to 2.9 MPa·m$^{1/2}$ after ~600 μm crack extension within the 80Al composition layer (residual tensile stress). However, as the crack extends into the 90Al composition layer (residual compressive stress), there is a steep increase to the *R*-curve. The calculated K_R profile, using the bridging stress function derived from the 80Al monolithic sample, closely follows the measured *R*-curve behavior of the sample.

The three calculated K_R profiles, shown in Fig. 4, differ from each other only in the estimated temperature range over which residual thermal stresses form (ΔT). The range of ΔT values of $1225° \pm 100°C$ shows that the differences in the three K_R profiles are small, and each continues to overlap the measured data. This suggests that the small errors in estimating ΔT do not result in large errors in the K_r profile and, thus, the calculated *R*-curve behavior.

IV. Discussion

(1) Estimating the Measured R-Curve

The weight function analysis can be used to predict the *R*-curve behavior only if the stress profiles ($\sigma_{bend}(x)$, $\sigma_r(x)$, and $\sigma_{br}(x')$) acting along the fracture path are estimated accurately.[37,38] The calculated K_R profile for the layered sample, as shown in Fig. 4, provides a good estimate of the measured *R*-curve behavior, suggesting that $\sigma_{bend}(x)$, $\sigma_r(x)$, and $\sigma_{br}(x')$ have been estimated reasonably well. The calculated stress intensity profiles (crack-tip toughness ($K_o(a)$), residual thermal ($K_r(a)$), and crack bridging ($K_{br}(a,a_o)$) show, in Fig. 2, how each contributes to the final $K_R(a,a_o)$ profile given in Fig. 4.

(2) Bridging Stress Distribution Estimates

The bridging stress function incorporates the Irwin *K*-field plane-strain displacement relation to estimate the COD as a distance behind the crack tip. However, this approximation does not include the influence of wake effects from the crack-bridging distribution on COD. Estimating the wake effect in homogenous materials is complex, and only by conducting COD measurements or knowing the crack-bridging closure stresses is one able to confirm the actual profile.[31,33] For alumina composites, the studies of Rödel *et al.*[31] and Sohn *et al.*[33] have demonstrated that the measured COD is less than the estimate from the Irwin *K*-field displacement relation. To account for this decrease in the COD caused by the bridging stress distribution acting along the crack, an additional function has been incorporated with the Irwin *K*-field function. However, only after iterative parametric adjustments are made to this new function is a calculated COD profile able to overlap the measured COD profile. Without the measured COD data, new COD functions, which account for the influence of wake effects, can be no more confidently predicted than those obtained using the Irwin *K*-field relation.

The bridging stress function derived from the 80Al monolithic sample is believed to include the influences of the bridging stress wake effects on COD, because the parameters σ_{max}, *n*, and *L* in Eq. (7) are estimated via curve fitting to the measured *R*-curve data. However, this stress function is then used to estimate the bridging stresses in the layered sample, and issues regarding the influence of the residual thermal stress distribution on K_{br} may become important. The residual thermal stress distribution is believed to influence the K_{br} profile by altering the COD along the crack length.

To estimate the errors in the K_{br} profile caused by the residual thermal stress distribution influence on COD, Eq. (6) has been modified by replacing K_o with $K_o - K_r$. For values of $K_r > 0$, residual tensile stress regions, the calculated COD is smaller than that for the no residual stress situation and results in an increased value for K_{br}. A decrease in COD results in an increase in *L*; the size of σ_{br} acting over the given crack length increases and, thus, K_{br} increases. The opposite is the case for $K_r < 0$. For the layered sample, if one considers the crack length of ~650 μm, the entire crack length has residual tensile stress acting along it, and, as shown in Fig. 2(b), $K_r = 1.5$ MPa·m$^{1/2}$. Using this value for K_r in the modified Eq. (6) results in $K_{br} \approx -1$ MPa·m$^{1/2}$; however, the calculated K_{br} for the no residual stress situation is approximately -0.8 MPa·m$^{1/2}$ (Fig. 2(c)), which suggests that the extent of this influence on the measured *R*-curve behavior is minor.

(3) Residual Stress Influence

The macroscopic residual thermal stress distribution acting within a sample dominates the measured *R*-curve behavior. The calculated stress intensity profiles in Fig. 2 show that the K_r profile has a variation of 2.8 MPa·m$^{1/2}$, whereas the K_o stress intensity

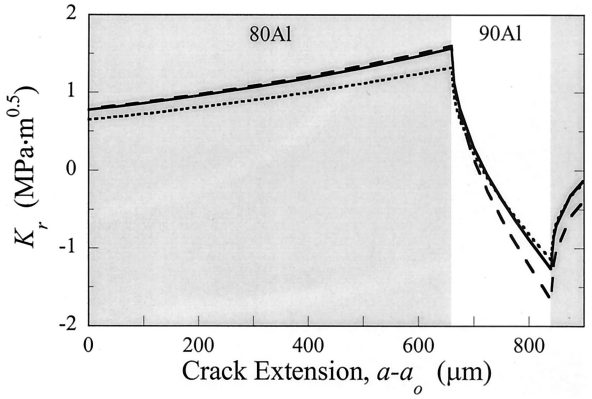

Fig. 5. Schematic of the estimated (– – –) K_r^{upper}, (- - -) K_r^{lower}, and (——) $K_r^{average}$ stress intensity factors as a function of position within the layered sample, calculated using material properties estimated by either the upper, lower, or geometric average of the upper and lower bounds of the rules-of-mixture, respectively (ΔT = 1225°C).

variation is only 0.4 MPa·m$^{1/2}$, and the K_{br} stress intensity variation is 0.9 MPa·m$^{1/2}$ after a 900 μm crack extension.

Moreover, comparing the measured *R*-curves for the 80Al and layered samples shows the influence of the residual stress distribution. For crack lengths less than ~650 μm in the layered sample (80Al composition layer), the measured *R*-curve should be almost identical to the one measured for the 80Al monolithic sample; however, because of the residual tensile stress acting in this composition layer (~10 MPa), the measured *R*-curve has a negative slope. For crack extensions into the 90Al composition region, the residual compressive stress (~120 MPa) results in the steep increase in the measured *R*-curve. The 90Al material *R*-curve slope is similar to that of the 80Al material because of similar grain size and compositions, and this suggests that the change in residual thermal stress alters the measured *R*-curve.

(4) Influence of Material Property Estimates on K_r

To evaluate the influence of the material properties estimates on the calculated K_r profile, a comparison was made between using E, ν, and α estimated by either the upper (equal strain), lower (equal stress), or geometric average of the upper and lower bounds of the rules-of-mixtures. Each material property-estimating scheme, with ΔT = 1225°C, resulted in slightly different K_r profiles, K_r^{upper}, K_r^{lower}, and $K_r^{average}$, respectively, and are shown in Fig. 5. The deviation between the three K_r profiles demonstrated the importance of accurate material property estimates. However, for the layered sample studied in this investigation, the small changes in the material properties between the three estimating methods resulted in only minor variations in the K_r profile. Each of the three K_r profiles could be used to estimate the K_R behavior of the layered sample, but the best fits to the measured *R*-curve data were obtained using $K_r^{average}$ with ΔT = 1225°C.

(5) Ramifications

The results of the current study may allow a new insight to differentiating the active toughening mechanisms resulting in the measured *R*-curve behavior of multilayered composites having residual stress distributions. The composite investigated by Marshall *et al.*,[3] which was described in the introduction, and by Marshall[39] is used as an example. The measured *R*-curve reported by Marshall *et al.*[3] and by Marshall[39]is shown in Fig. 6 along with the K_r profile that was calculated from the residual stress distribution (including tile warping) induced by differences in the thermal expansion coefficient between the 100Z and 50Z compositional layers. K_r was calculated using material properties that were estimated by the geometric average of the upper and lower bounds of the rule-of-mixtures and ΔT = 1225°C. The resulting residual stress distribution, ~40 MPa tensile stress within the 100Z regions and ~600 MPa compressive stress within the 50Z layers, is expected to have a significant influence on the measured *R*-curve behavior of this sample.

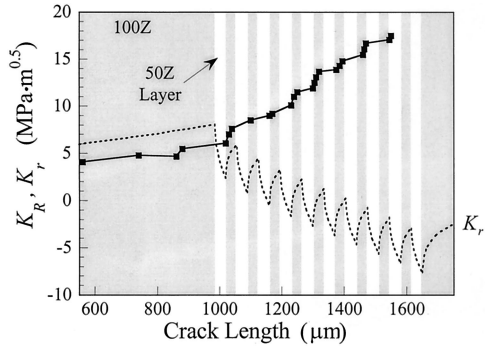

Fig. 6. SEPB-measured *R*-curve of the layered sample reported by Marshall *et al.*[2] with the calculated K_r (not K_R) profile superimposed, showing that the residual thermal stress may have a significant contribution to the measured *R*-curve.

For the layered sample in the current study, the K_r profile directly showed how the residual stress distribution influenced the measured *R*-curve behavior. The resulting K_r profile plotted in Fig. 6 shows the amount of crack-tip shielding that was induced by the residual compressive stress distribution occurring within the layered region. The residual stress distribution in the composite investigated by Marshall *et al.* appears to be at least partially responsible for the increase in the measured *R*-curve within the layered region of the sample.

V. Conclusions

(1) The weight function analysis demonstrates that the macroscopic residual stress distribution acting within a sample can have a significant influence on the measured *R*-curve behavior.

(2) The weight function analysis can be used to predict the *R*-curve behavior of layered composites only if the stress profiles ($\sigma_{bend}(x)$, $\sigma_r(x)$, and $\sigma_{br}(x')$) acting along the fracture path are accurately estimated.

Appendix

$$E_1 = \int_0^W E'(x)\,dx \tag{A–1}$$

$$E_2 = \int_0^W xE'(x)\,dx \tag{A–2}$$

$$E_3 = \int_0^W x^2E'(x)\,dx \tag{A–3}$$

$$A_1 = \int_0^W \alpha(x)E'(x)\,dx \tag{A–4}$$

$$A_2 = \int_0^W x\alpha(x)E'(x)\,dx \tag{A–5}$$

where $E'(x)$ is the elastic modulus corrected for plane strain.

Acknowledgment

The authors thank Martin Stech and Emil Aulbach for experimental assistance.

References

[1]R. Lakshminarayanan, D. Shetty, and R. Cutler, "Toughening of Layered Ceramic Composites with Residual Surface Compression," *J. Am. Ceram. Soc.*, **79** [1] 79–87 (1996).

[2]A. J. Blattner, R. Lakshminarayanan, and K. K. Shetty, "Toughening of Layered Ceramic Composites with Residual Surface Compression: Effects of Layer Thickness," *Eng. Fract. Mech.*, **68**, 1–7 (2001).

[3]D. Marshall, J. Ratto, and F. Lange, "Enhanced Fracture Toughness in Layered Microcomposites of Ce-ZrO_2 and Al_2O_3," *J. Am. Ceram. Soc.*, **74** [12] 2979–87 (1991).

[4]O. Prakash, P. Sarkar, and P. S. Nicholson, "Crack Deflection in Ceramic/Ceramic Laminates with Strong Interfaces," *J. Am. Ceram. Soc.*, **78** [4] 1125–27 (1995).

[5]M. Y. He, A. G. Evans, and J. W. Hutchinson, "Crack Deflection at an Interface Between Dissimilar Elastic Materials: Role of Residual Stress," *Int. J. Solids Struct.* **31** [24] 3443–55 (1994).

[6]M. P. Rao, A. J. Sánches-Herencia, G. E. Beltz, R. M. McMeeking, and F. F. Lange, "Laminar Ceramics that Exhibit a Threshold Strength," *Science (Washington, DC)*, **286**, 102–105 (1999).

[7]H.-J. Yu, J.-L. Wan, K.-M. Liang, Da-Ningwang, and F.-R. Liu, "Toughening and Transformation of 14 mol% Ce-TZP and Al_2O_3/Ce-TZP Layered Micro-Composites," *J. Mater. Sci. Lett.*, **88**, 1965–67 (1999).

[8]H. Tomaszewski, J. Strzeszewski, and W. Gebicki, "The Role of Residual Stresses in Layered Composites of Y-ZrO_2 and Al_2O_3," *J. Eur. Ceram. Soc.*, **19**, 255–62 (1999).

[9]R. Moon, K. Bowman, K. Trumble, and J. Rödel, "A Comparison of *R*-Curves from SEVNB and SCF Fracture Toughness Test Methods on Multilayered Alumina–Zirconia Composites," *J. Am. Ceram. Soc.*, **83** [2] 445–47 (2000).

[10]R. J. Moon, K. Bowman, K. Trumble, and J. Rödel, "Fracture Resistance Curve Behavior of Multilayered Alumina–Zirconia Composites Produced by Centrifugation," *Acta Mater.*, **49** [6] 995–1003 (2001).

[11]R. J. Moon, "Static Fracture Behavior of Multilayer Alumina–Zirconia Composites"; Ph.D. Thesis. Purdue University, West Lafayette, IN, May 2000.

[12]J. C. Chang, B. V. Velamakanni, F. F. Lange, and D. S. Pearson, "Centrifugal Consolidation of Al_2O_3 and Al_2O_3/ZrO_2 Composite Slurries vs Interparticle Potentials: Particle Packing and Mass Segregation," *J. Am. Ceram. Soc.*, **74** [9] 2201–204 (1991).

[13]W. Huisman, T. Graule, and L. J. Gauckler, "Alumina of High Reliability by Centrifugal Casting," *J. Eur. Ceram. Soc.*, **15**, 811–21 (1995).

[14]J. Chang, F. Lange, and D. Pearson, "Pressure Sensitivity for Particle Packing of Aqueous Al_2O_3 Slurries vs Interparticle Potential," *J. Am. Ceram. Soc.*, **77** [5] 1357–60 (1994).

[15]O. Sbaizero and E. Lucchini, "Influence of Residual Stresses on the Mechanical Properties of a Layered Ceramic Composite," *J. Eur. Ceram. Soc.*, **16**, 813–18 (1996).

[16]B. V. Velamakanni, J. C. Chang, F. F. Lange, and D. S. Pearson, "New Method for Efficient Colloidal Particle Packing via Modulation of Repulsive Lubrication Hydration Forces," *Langmuir*, **6** [7] 1323–25 (1990).

[17]J. Kübler, "Fracture Toughness Using the SEVNB Method: Preliminary Results," *Ceram. Eng. Sci. Proc.*, **18** [4] 155–62 (1997).

[18]M. Stech and J. Rödel, "Method for Measuring Short-Crack *R*-Curves without Calibration Parameters: Case Studies on Alumina and Alumina/Aluminum Composites," *J. Am. Ceram. Soc.*, **79** [2] 291–97 (1996).

[19]H. F. Bueckner, "A Novel Principle for the Computation of Stress Intensity Factors," *Z. Angew Math. Mech.*, **50**, 529–46 (1970).

[20]T. Fett and D. Munz, "Influence of Crack–Surface Interactions on Stress Intensity Factor in Ceramics," *J. Mater. Sci. Lett.*, **9**, 1403–406 (1990).

[21]T. Fett and D. Munz, "Determination of Fracture Toughness at High Temperature after Subcritical Crack Extension," *J. Am. Ceram. Soc.*, **75** [11] 3133–36 (1992).

[22]T. Fett, "Determination of Residual Stresses in Components Using the Fracture Mechanics Weight Function," *Eng. Fract. Mech.*, **55** [4] 571–76 (1996).

[23]T. Fett, D. Munz, and Y. Y. Yang, "Direct Adjustment Procedure for Weight Function Analysis of Graded Materials," *Fatigue Fract. Eng. Mater. Struct.*, **23**, 191–98 (2000).

[24]T.-J. Chung, A. Neubrand, J. Rödel, and T. Fett, "Fracture Toughness and *R*-Curve Behavior of Al_2O_3/Al FGMs"; pp. 789–96 in Ceramic Transactions, Vol. 114, *Functionally Graded Materials 2000*. Edited by K. Trumble, K. Bowman, I. Reimanis, and S. Sampath. American Ceramic Society, Westerville, OH, 2002.

[25]R. J. Moon, M. Hoffman, J. Hilden, K. Bowman, K. Trumble, and J. Rödel, "*R*-Curve Behavior in Alumina–Zirconia Composites with Repeating Graded Layers," *Eng. Fract. Mech.*, in press.

[26]J. D. French, J. Zhao, M. P. Harmer, H. M. Chan, and G. A. Miller, "Creep of Duplex Microstructures," *J. Am. Ceram. Soc.*, **77** [11] 2857–65 (1994).

[27]P. Z. Cai, D. J. Green, and G. L. Messing, "Constrained Densification of Alumina/Zirconia Hybrid Laminates: II, Viscoelastic Stress Computation," *J. Am. Ceram. Soc.*, **80** [8] 1940–48 (1997).

[28]Y.-W. Mai and B. R. Lawn, "Crack–Interface Grain Bridging as a Fracture Resistance Mechanism in Ceramics: II, Theoretical Fracture Mechanics Model," *J. Am. Ceram. Soc.*, **70** [4] 289–94 (1987).

[29]S. Bennison and B. Lawn, "Role of Interfacial Grain-Bridging Sliding Friction in the Crack-Resistance and Strength Properties of Nontransforming Ceramics," *Acta Metall.*, **37** [10] 2659–71 (1989).

[30]R. Steinbrech, A. Reichl, and W. Schaarwächter, "*R*-Curve Behavior of Long Cracks in Alumina," *J. Am. Ceram. Soc.*, **73** [7] 2009–15 (1990).

[31]J. Rödel, J. F. Kelly, and B. R. Lawn, "*In Situ* Measurements of Bridged Crack Interfaces in the Scanning Electron Microscope," *J. Am. Ceram. Soc.*, **73** [11] 3313–18 (1990).

[32]J. C. Hay and K. W. White, "Grain-Bridging Mechanisms in Monolithic Alumina and Spinel," *J. Am. Ceram. Soc.*, **76** [7] 1849–54 (1993).

[33]K.-S. Sohn, S. Lee, and S. Baik, "Analytical Modeling for Bridging Stress Function Involving Grain Size Distribution in a Polycrystalline Alumina," *J. Am. Ceram. Soc.*, **78** [5] 1401–405 (1995).

[34]C. J. Gilbert and R. O. Ritchie, "On the Quantification of Bridging Tractions During Subcritical Crack Growth Under Monotonic and Cyclic Fatigue Loading in a Grain-Bridging Silicon Carbide Ceramic," *Acta Metall.*, **46** [2] 609–16 (1998).

[35]G. I. Barenblatt, "The Mechanical Theory of Equilibrium Cracks in Brittle Fracture," *Adv. Appl. Mech.*, **20** [3] 55–129 (1962).

[36]E. H. Lutz, N. Claussen, and M. V. Swain, "K_R-Curve Behavior of Duplex Ceramics," *J. Am. Ceram. Soc.*, **74** [1] 11–18 (1991).

[37]T. Fett, D. Munz, and G. Thun, "Evaluation of Bridging Parameters in Aluminas from *R*-Curves by Use of the Fracture Mechanical Weight Function," *J. Am. Ceram. Soc.*, **78** [4] 949–51 (1995).

[38]T. Fett, D. Munz, C.-T. Yu, and A. S. Kobayashi, "Determination of Bridging Stresses in Reinforced Al_2O_3," *J. Am. Ceram. Soc.*, **77** [12] 3267–69 (1994).

[39]D. B. Marshall, "Design and Properties of Multilayered Ceramic Composites," *Mater. Res. Soc. Symp. Proc.*, **434**, 195–203 (1996).

[40]C. Hillman, Z. Suo, and F. F. Lange, "Cracking of Laminates Subjected to Biaxial Tensile Stresses," *J. Am. Ceram. Soc.*, **79** [8] 2127–33 (1996).

[41]R. G. Munro, "Evaluated Material Properties for a Sintered α-Alumina," *J. Am. Ceram. Soc.*, **80** [8] 1919–28 (1997). □